Microbial U isotope fractionation depends on U(VI) reduction rate

Journal:	*Environmental Science & Technology*
Manuscript ID	es-2019-05935c.R1
Manuscript Type:	Article
Date Submitted by the Author:	30-Dec-2019
Complete List of Authors:	Basu, Anirban; Royal Holloway University of London, Department of Earth Sciences Wanner, Christoph; University of Bern Institute of Geological Sciences Johnson, Thomas; University of Illinois at Urbana-Champaign, Department of Geology Lundstrom, Craig; University of Illinois at Urbana-Champaign, Department of Geology Sanford, Robert; University of Illinois at Urbana-Champaign, Department of Geology Sonnenthal, Eric ; Lawrence Berkeley National Laboratory Boyanov, Maxim; Argonne National Laboratory, Biosceinces Division Kemner, Kenneth; Argonne National Laboratory, Biosceinces Division

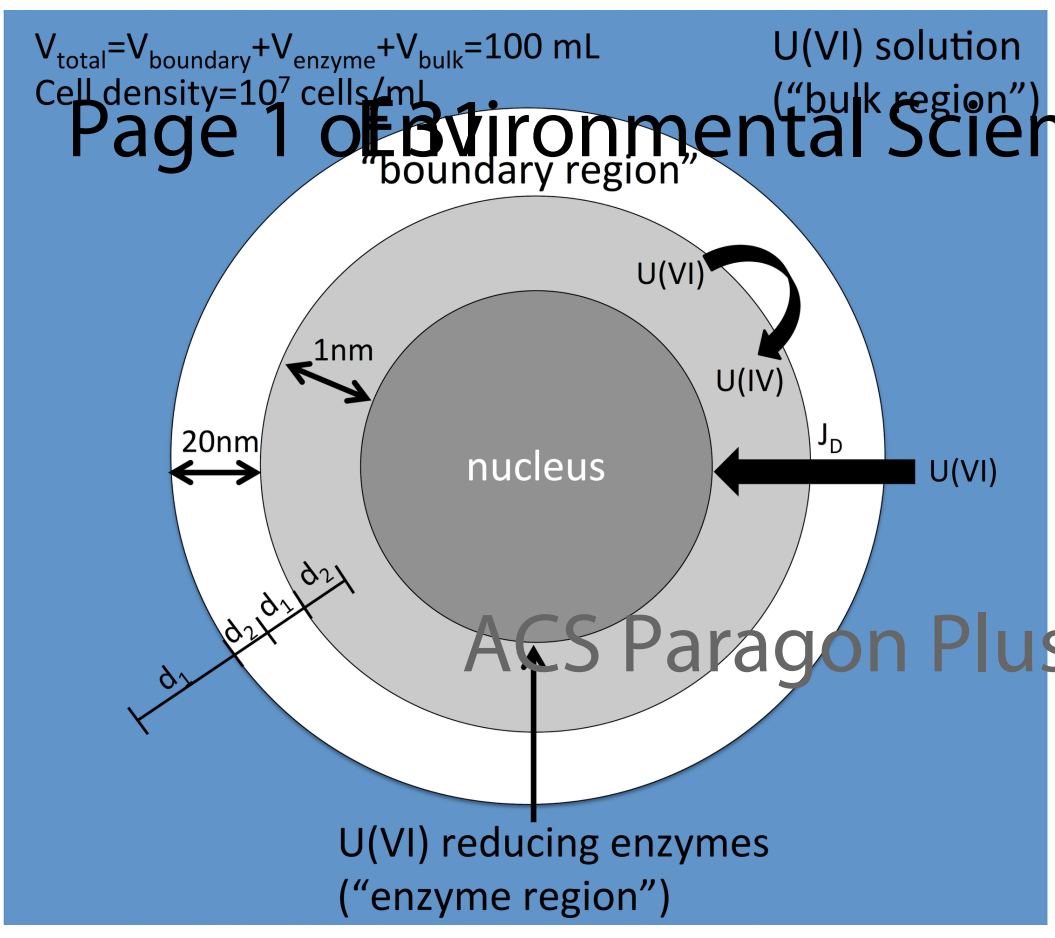

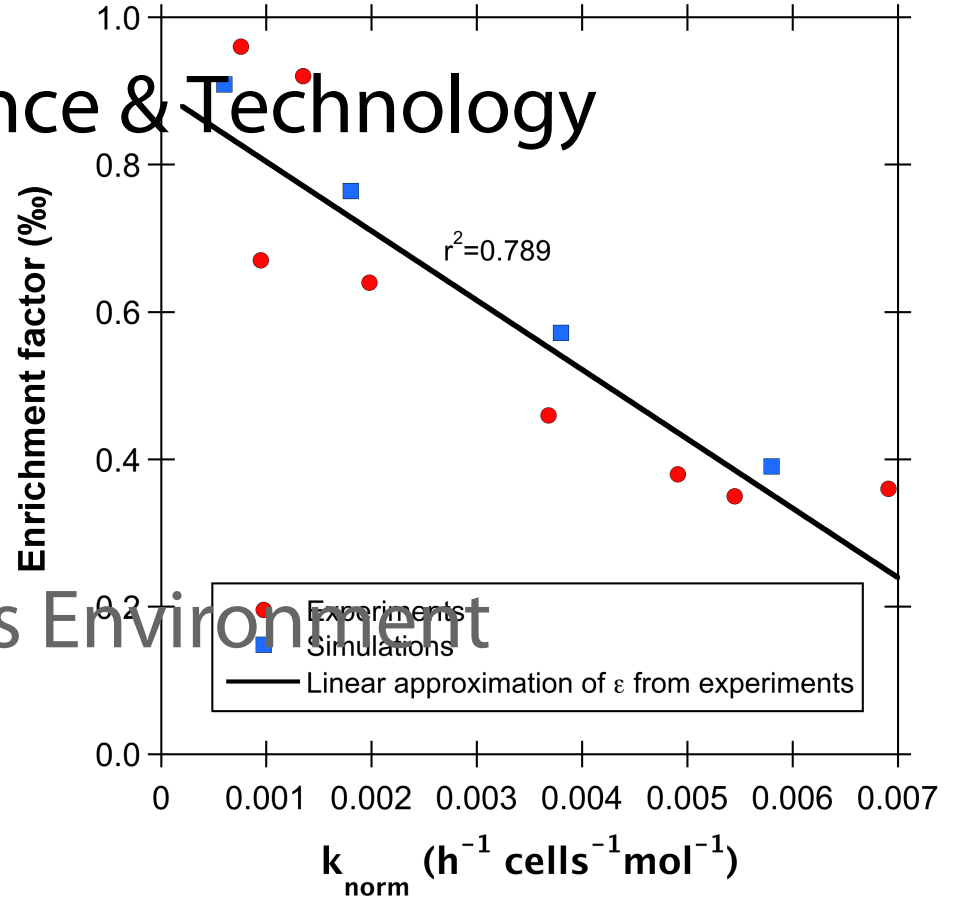

Microbial U isotope fractionation depends on U(VI) reduction rate

Anirban Basu[1], Christoph Wanner[2], Thomas M. Johnson[3], Craig C. Lundstrom[3], Robert A. Sanford[3], Eric L. Sonnenthal[4], Maxim I. Boyanov[5,6], Kenneth M. Kemner[5]*

1. Department of Earth Sciences, Royal Holloway, University of London, Egham, UK, TW20 0EX

2. Institute of Geological Sciences, University of Bern, Baltzerstrasse 3, CH-3012, Switzerland

3. Department of Geology, University of Illinois at Urbana-Champaign, Urbana, IL, USA 61801

4. Lawrence Berkeley National Laboratory, 1 Cyclotron Road, Berkeley, CA, USA, 94720

5. Biosciences Division, Argonne National Laboratory, Argonne, IL, USA, 60439

6. Bulgarian Academy of Sciences, Institute of Chemical Engineering, Sofia 1113, Bulgaria

KEYWORDS: Uranium isotopes, bacteria, U(VI) reduction rate, numerical simulations

ABSTRACT

U isotope fractionation may serve as an accurate proxy for U(VI) reduction in both modern and ancient environments, if the systematic controls on magnitude of fractionation (ε) are known. We model the effect of U(VI) reduction kinetics on U isotopic fractionation during U(VI) reduction by a novel *Shewanella* isolate, *Shewanella* sp. (NR) in batch incubations. The measured ε values range from 0.96 ‰ ± 0.16 to 0.36 ‰ ± 0.07 ‰ and are strongly dependent on the U(VI) reduction rate. The ε decreases with increasing reduction rate constants normalized by cell density and initial U(VI). Reactive transport simulations suggest that the rate dependence of ε is due to a two-step process, where diffusive transport of U(VI) from the bulk solution across a boundary layer is followed by enzymatic reduction. Our results imply that the spatial decoupling of bulk U(VI) solution and enzymatic reduction should be taken into account for interpreting U isotope data from the environment.

INTRODUCTION

The uranium isotope ratio $^{238}U/^{235}U$ is an effective proxy for understanding microbially-mediated uranium (U) reduction, which is an integral part of the global U cycling throughout geologic time. Bacterial reduction of soluble U(VI) to insoluble U(IV) leads to preferential partitioning of ^{238}U in the U(IV) solids with lowest possible electron density configuration at the nucleus[1-3]. This equilibrium isotopic exchange resulting from the differences in nuclear size and shape is described in the literature as a nuclear volume effect (NVE)[4,5]. However, it is not clear how and at which rate the exchange occurs during kinetically controlled and irreversible microbial reduction. With continued bacterial reduction, the residual aqueous U(VI) becomes progressively enriched in ^{235}U. Direct measurement of $^{238}U/^{235}U$ permits the quantification of U cycling in both modern and ancient environments such as contaminated aquifers[6,7] and the rock

record[8], but this is predicated on a robust understanding of the factors that control the magnitude of U isotopic fractionation during microbial U(VI) reduction.

The magnitude of U isotope fractionation caused by bacterial U(VI) reduction is variable. Generally, it is expressed as the enrichment factor ε (ε (‰) = 1000*(α−1); $\alpha = (R_{\text{instantaneous U(IV) product}}/R_{U(VI)})$ where R is $^{238}U/^{235}U$). A field-scale biostimulation of a U(VI) contaminated aquifer at Rifle, CO, USA, has yielded an apparent fractionation (as ε) of 0.46‰[9]. Laboratory batch incubations with a diverse group of bacteria have revealed a range of ε from 0.7‰ to 1.0‰[1]. Subsequent experimental work has reported a similar range for batch incubations with single strains[2,3]. The large variability of ε translates to large uncertainties in determining the fraction of reduction of toxic U(VI) in contaminated aquifers[9-11] or the extent of anoxia in ancient oceans[12], which makes the interpretation of the environmental U isotope data equivocal. To date, the origins and nature of variability of ε for microbial U(VI) reduction has not been fully explored. For similar redox-active elements like S and N, however, the variation of ε is systematically controlled by the rate of microbial sulfate and nitrate reduction (e.g. ref. [13,14]).

The key role of bacterial physiology in controlling the S isotopic fractionation by sulfate reducers is well understood[13,15,16]. One crucial factor that controls the S isotope fractionation is the balance between the rate of sulfate delivery into the cell and the rate of sulfate reduction in the cell[13,17]. The fractionation is maximized when the transport of sulfate into the cell is unlimited and the electron donor supply is limited leading to slow reduction[13]. In contrast, when the supply of sulfate is low relative to the supply of the electrons such that the supplied sulfate is rapidly, and nearly quantitatively, reduced, the S isotopic fractionation diminishes to zero. The balance between the reduction rate and supply of sulfate depends on the components of enzymatic reaction machinery and the electron transport chain. Similarly, we expect that

63 microbial U isotopic fractionation may be influenced by the rate of U(VI) reduction relative to
64 the rate of U(VI) supply, despite differences in mechanisms of U(VI) reduction and cellular
65 transport of U(VI).

66 Bacterial strains from the *Shewanella* genera are particularly well-studied for their U(VI)
67 reduction ability, which has generally been attributed to membrane-associated enzymes –c-type
68 cytochromes associated with the outer membrane or the periplasmic space[18-22]. Consequently, the
69 U(IV) reaction products are observed to form outside the cell, on the cell membrane and in the
70 periplasmic space in several *Shewanella* species[21,23]. Therefore, the localization of U(VI)
71 reduction in the vicinity of the outer-membrane or periplasmic enzymes may influence the
72 balance between the U(VI) delivery and reduction rate.

73 Here we demonstrate the effect of variable U(VI) reduction rates on the magnitude of isotopic
74 fractionation in batch incubation experiments with *Shewanella* sp. (NR). We varied the initial
75 U(VI) concentration while keeping other parameters (e.g. electron donor concentration, cell
76 density) the same and we determined the magnitude of isotopic fractionation. We propose a two-
77 step mechanistic model of U isotopic fractionation with diffusive delivery of aqueous U(VI)
78 followed by enzymatic U(VI) reduction. In this model, we consider a diffusive boundary layer
79 surrounding the cell separating a region of enzymatic reduction from the bulk U(VI) solution.
80 We test this conceptual model by reactive transport simulations of U(VI) reduction by
81 *Shewanella* sp. (NR) to demonstrate the role of reaction kinetics in controlling the overall
82 isotopic fractionation.

83 METHODS

84 ***Media for Bacterial Cultures and U(VI) Incubations***

Shewanella sp. (NR) cultures were grown anaerobically in 80-100 mL batch cultures at 30°C using a mineral-salt media described in ref. [1]. Briefly, the medium contained 200 μM phosphate and 10 mM of HCO_3^- buffer with a final pH of 7.2. The cultures were grown on 2.5 mM lactate as electron donor and 1 mM NO_3^- as electron acceptor. The medium for U(VI) incubation experiments was identical to the growth medium except that the phosphate concentration was lowered to 20 μM to avoid abiotic U(VI)-phosphate precipitation. All reductants, vitamin solution and resazurin were omitted from both growth and test medium.

U(VI) Incubation Experiments

A uranyl carbonate solution in 100 mM $NaHCO_3$, prepared from Uranium (normal) metal CRM 112-A, was routinely used as U(VI) stock solution for desired initial U(VI) concentration in our experiments[1]. Each experiment was conducted in duplicate. A ~10 mL inoculum (10% v/v) of pre-grown *Shewanella* sp. (NR) was used for each experiment. The density of the microbial population in each reactor and the inoculum was quantified using a LSR II (BD Biosciences) flow cytometry analyzer. Abiotic control experiments with the test medium, the U(VI) bicarbonate solution and no bacteria were conducted for selected initial U(VI) concentrations. All reactors were supplemented with 500 μM of lactate as the electron donor. During the course of the experiments, all reactors were incubated at 30°C in the dark, shaken constantly at 125 rpm. Each reactor was sampled for U(VI) concentrations and U isotopes at regular intervals. The samples were filtered using 0.2 μm filters and stored at 4°C prior to analyses.

U Concentration and Isotope Measurements

For isotopic analysis, we used a $^{233}U + ^{236}U$ double isotope spike technique to correct for any isotopic fractionation arising from sample purification or mass bias of the instrument during

mass-spectrometry. An aliquot of double isotope spike solution, composed of ^{236}U and ^{233}U, was added to each sample prior to sample purification by UTEVA resin [1,6,7,9,24,25]. Reported U(VI) concentrations were determined from isotope dilution calculations using measurements of spike isotopes and natural U isotopes in the samples. The $\delta^{238}U$ values were measured using a Nu Plasma HR MC-ICP-MS. The precision of the isotopic measurements was 0.07‰, determined using a modified root mean square calculation[26] for 9 pairs of full procedural duplicate sample preparations. The relationship between isotopic composition and concentration from each set of U(VI) incubations was determined using a Rayleigh distillation equation

$$\delta_t = (\delta_0 + 1000‰)[\frac{c_t}{c_0}]^{\alpha - 1} - 1000‰ \quad (1)$$

where c_0 and $\delta_0$are the initial concentration and isotopic composition of U(VI), c_t and are δ_t the concentration and isotopic composition at time t, and α is the isotopic fractionation factor. The α values were calculated from the slope of the best fit line from linearized plots of $\ln(\delta^{238}U + 1000‰)$ vs. $\ln(c_t)$[27]. The uncertainties of ε (2*standard error) were derived from the uncertainties of the slopes from data scatter about the best-fit lines using linear estimation method.

For experiments with early rapid U(VI) reduction, the sample taken a few minutes into each experiment is used as the effective starting point for $\delta^{238}U$ and U(VI) concentration (see SI for more details). We also exclude some data from time points close to the completion of the reduction (e.g. >88% reduction for the experiment with $U(VI)_{t=0}$ = 18.2 μM) from our isotopic analysis. These data points are aberrantly shifted towards isotopically heavier values, which may be attributed to the contamination of the dissolved U(VI) solution by very fine U(IV) particles that later oxidize to U(VI).

Characterization of U(IV) precipitates

Solid-phase associated U in the reactors was separated using a 0.2 μm filter and analyzed using Uranium L_{III}-edge X-ray absorption near-edge structure (XANES) at the MRCAT/EnviroCAT beamline, Advanced Photon Source, Argonne National Laboratory. The details of the analysis can be found in ref. [28] .

Reactive transport modeling

A series of reactive transport model simulations using TOUGHREACT V3[29] in combination with the EQ3/6 thermodynamic database[30] as well as uraninite solubility data taken from ref. [31] is performed to simulate U(VI) reduction and associated U isotopic fractionation. TOUGHREACT has been widely applied to evaluate isotopic fractionation coupled to water-rock interaction and biogeochemical processes in a variety of subsurface environments and laboratory experiments[32,33]. Furthermore, the TOUGHREACT approach for simulating isotopic fractionation coupled to redox reactions has been recently benchmarked[34].

Conceptual Model

Our simplified conceptual model considers that cells are surrounded by boundary layers with U(VI) concentrations lower than those in the bulk solution (Fig. 1). Consequently, for our simulations we assume that U(VI) reduction occurs as a two-step process with (i) diffusive U(VI) transport through boundary layers and (ii) enzymatic U(VI) reduction at the cell surface or within the periplasmic space. A similar conceptual approach was successfully used by ref.[32] to demonstrate that Cr isotopic fractionation inherited from Cr(VI) reduction is muted if the reduction rate is high and/or diffusive transport is slow.

Model Setup

U(VI) reduction and associated U isotopic fractionation is simulated for a static batch reactor with no flow. A multi-region approach[35] is used to numerically formulate the conceptual model

(Fig. 1). To do so, the batch reactor is discretized into three different regions: (i) a bulk region corresponding to the U(VI) solution that is continuously sampled during the experiment, (ii) an enzyme region with enzymatic U(VI) reduction and (iii) a boundary region separating the previous two.

The physical parameters defined for the three regions are listed in Table S2 (Supporting Information). The simulations are performed for a model volume of 100 mL similar to that of the experiments. The volumes of the individual regions and mutual interfaces are defined assuming a cell density of 10^7 cells/mL, which is the average cell density of our experiments; a cuboid shape of *Shewanella* with a diameter of 0.6 μm and length of 3.4 μm[36]; and a boundary layer thickness of 20 nm. Although 20 nm approximately corresponds to the thickness of the entire Gram negative membrane of *Shewanella*[37], we aim to simulate a general case where the location of U(VI) reduction is physically separated from the bulk U(VI) solution.

The cell density is kept constant during our simulations, meaning that we do not simulate microbial growth occurring in our experiments. The diffusive flux of U(VI) (J_D) through the individual regions of our model (Fig. 1) is calculated according to

$$J_D = D_{aq}.\tau.\phi.\frac{A}{d_1 + d_2}.\frac{dC}{dx} \quad (2)$$

where D_{aq} refers to the diffusion coefficient of aqueous species, A (m^2) is the interfacial area between two adjacent regions, $\frac{dC}{dx}$ refers to the U(VI) concentration gradient across a region ($mol/kg_{H2O}/m$), d_1 and d_2 refer to the distances from the centers of two adjacent regions to their mutual interface (Fig. 1), τ is the tortuosity, and ϕ is the porosity, which was set to 0.99. For the simulations it was assumed that the bulk region is fully mixed because the experiments were continuously stirred. Accordingly, the tortuosity of the bulk region was set to a very high value

of 10^8. A value of 10^8 was also defined for the 1 nm thick enzyme region because we assume that U(VI) is not further diffusively transported once it reaches a particular enzyme.

Reaction network

U(VI) reduction to U(IV) was assumed to occur exclusively within the enzyme region of our model (Fig. 1). It was simulated as a kinetic reaction with lactate ($C_3H_5O_3^-$) under the production of HCO_3^- and acetate ($C_2H_3O_2^-$) assuming that U(IV) immediately precipitates as uraninite ($UO_{2(s)}$). To simulate the fate of ^{238}U and ^{235}U, U(VI) reduction was defined for the two dominating U(VI) and U(IV) isotopologues:

$$0.5\ C_3H_5O_3^- + (^{235}UO_2)^{2+} + H_2O = {}^{235}UO_{2(s)} + 0.5\ HCO_3^- + 0.5\ C_2H_3O_2^- + 2.5\ H^+ \quad (3)$$

$$0.5\ C_3H_5O_3^- + (^{238}UO_2)^{2+} + H_2O = {}^{238}UO_{2(s)} + 0.5\ HCO_3^- + 0.5\ C_2H_3O_2^- + 2.5\ H^+ \quad (4)$$

$^{235}UO_{2(s)}$ and $^{238}UO_{2(s)}$ are defined as endmembers of an ideal uraninite solid solution with an overall precipitation rate ${}^{ss}r$ (mol kg_{H2O}^{-1} s^{-1}) corresponding to the sum of the precipitation rate of the two endmembers (${}^{235UO2(s)}r$ and ${}^{238UO2(s)}r$)

$$^{ss}r = {}^{235UO_{2(s)}}r + {}^{238UO_{2(s)}}r \quad (5)$$

The precipitation rate for the $^{235}UO_{2(s)}$ and $^{238}UO_{2(s)}$ endmembers is calculated according to a transition state theory type rate law

$$^{235UO_{2(s)}}r = A \cdot k \left(1 - \frac{Q_{^{235}UO_{2(s)}}}{K_{^{235}UO_{2(s)}}} \right) + k_{UO_{2(s)}} \cdot A \left(x_{^{235}UO_{2(s)}} - 1 \right) \quad (6)$$

$$^{238UO_{2(s)}}r = A \cdot k \left(1 - \frac{Q_{^{238}UO_{2(s)}}}{K_{^{238}UO_{2(s)}}} \right) + k_{UO_{2(s)}} \cdot A \left(x_{^{238}UO_{2(s)}} - 1 \right) \quad (7)$$

where A ($m^2_{mineral}/kg_{H2O}$) and $k_{UO2(s)}$ (mol kg_{H2O}^{-1} m^{-2} s^{-1}) refer to the reactive surface area and the reaction rate constant of the solid solution, respectively (Table S3), $Q_{235UO2(s)}$ and $Q_{238UO2(s)}$ are the ion activity products of reactions 3 and 4, $K_{235UO2(s)}$ and $K_{238UO2(s)}$ refer to the

corresponding equilibrium constants (Table S3), and $x_{235UO2(s)}$ and $x_{238UO2(s)}$ are the mole fractions of the precipitating end-members. To ensure that the volume ratio of these endmembers reflect the fluid composition, $x_{235UO2(s)}$ and $x_{238UO2(s)}$ are calculated according to

$$x_{^{235}UO_{2(s)}} = \frac{Q_{^{235}UO_{2(s)}} / K_{^{235}UO_{2(s)}}}{Q_{^{235}UO_{2(s)}} / K_{^{235}UO_{2(s)}} + Q_{^{238}UO_{2(s)}} / K_{^{238}UO_{2(s)}}} \quad (8)$$

$$x_{^{238}UO_{2(s)}} = \frac{Q_{^{238}UO_{2(s)}} / K_{^{238}UO_{2(s)}}}{Q_{^{235}UO_{2(s)}} / K_{^{235}UO_{2(s)}} + Q_{^{238}UO_{2(s)}} / K_{^{238}UO_{2(s)}}} \quad (9)$$

By setting $K_{238UO2(s)}/K_{235UO2(s)} = 1.001$ and by using a constant reactive surface area A and a reaction rate constant $k_{UO2(s)}$ (eqs. (6) and (7)) we run our simulations with an intrinsic equilibrium ε of 1.0‰ (Table S3).

Initial conditions

The chemical composition initially specified for the three regions of the model (Fig. 1) as well as the variation of the uraninite reaction rate constant with decreasing $U(VI)_{t=0}$ are listed in Tables S4 and S5.

RESULTS AND DISCUSSIONS

U concentration and Isotopic measurements

The U(VI) concentrations and $\delta^{238}U$ measured at regular time intervals in batch incubations are shown in Fig. 2. No significant U(VI) removal in control experiments indicates that the test medium does not abiotically reduce U(VI). The X-ray Absorption Near Edge Structure (XANES) analysis of the solid reaction products from the experiments confirms that ~90% of the U is reduced to U(IV) (Fig. 3). A first order kinetic model reasonably fits the U(VI) concentration data from each reactor, except for the latest time points. The half-lives of U(VI)

($t_{1/2}$ = ln(2)/k, k = first-order rate constant) range from 15 h to 45 h. The normalized first-order rate constants [k_{norm}, defined as $k_{firstorder}$/(cell density * $U(VI)_{t=0}$)] vary from 0.0008 to 0.007 $h^{-1}cells^{-1}mol^{-1}$ and decrease linearly with increasing initial U(VI) concentration (r^2=0.762, Fig. S1).

The $\delta^{238}U$ values of the aqueous U(VI) decreased steadily relative to the starting $\delta^{238}U$ composition (~0.0‰) to a minimum of –1.52‰ after 67% reduction (Fig. 2, Table S1). The ε values are determined by fitting the data from each reactor to a Rayleigh distillation model. For each experiment, a single ε fits all data from duplicate experiments. The resulting ε values vary from 0.36‰ to 0.96‰ (Fig. 2, Table S1) and decrease linearly with increasing k_{norm} (r^2=0.789, Fig. 4), meaning that slower U(VI) reduction yields stronger isotopic fractionation. The uncertainties (2σ) of ε values of the duplicate experiments combined range from ±0.07 to ±0.16‰.

Reactive transport modeling results

The first simulation is performed for an initial U(VI) concentration ($^{238}U(VI)$ + $^{235}U(VI)$) of 18 μM while the initial $\delta^{238}U$ value is set to 0.0‰ according to the starting $\delta^{238}U$ of U(VI). An intrinsic ε of 1.0‰ is defined for enzymatic U(VI) reduction, which roughly corresponds to the maximum ε observed in our experiments. The chemical composition initially specified for the three regions of the model is given in Table S4. The diffusion coefficients for $^{235}U(VI)$, $^{238}U(VI)$, and all other aqueous species are set to 10^{-9} m^2 s^{-1}. A good match between experimental data and simulation results is achieved by numerically calibrating the rate constant of the specified U(VI) reduction reaction and the tortuosity of the boundary layer (Fig. 5, 6).

After calibrating the model, simulations are run for initial U(VI) concentrations of 15, 10, and 5 μM. The reaction rate constants for computing U(VI) reduction are adjusted according to the correlation observed between k_{norm} and the initial U(VI) concentration (Fig. S1). All other

241 parameters are kept the same as in the simulations performed for $U(VI)_{t=0}$ =18 μM. For all initial
242 U(VI) concentrations, $\delta^{238}U$ decreases with progressive U(VI) reduction. When plotted against
243 the fraction of reduction (ln(*f*)), simulated $\delta^{238}U$ values in the bulk region plot on perfectly
244 straight lines (r^2=1) (Fig. 7). This demonstrates that U isotopic fractionation during U(VI)
245 reduction follows a Rayleigh type distillation with an effective ε that varies between the
246 simulations despite defining a constant input ε of 1.0‰. Therefore, a Rayleigh type model is
247 applied to calculate the effective ε for all our simulations, which corresponds to the slope of the
248 best-fit lines on $\delta^{238}U$ vs. ln(*f*) plots. The ε derived from the simulations also decreases with
249 increasing k_{norm} and matches very well with the ε derived from the experimental data (Fig. 4).

250 ***Rate dependence of U Isotopic fractionation***

251 Similar to microbial S or N isotopic fractionation, the dependence of U isotopic fractionation
252 on U(VI) reduction rate suggests a diffusive barrier between the reaction site and the bulk U(VI)
253 pool. The diffusive barriers may arise from surface coatings of extracellular polymeric
254 substances (EPS) enveloping the cell[38-40] or from the cell membrane if a substantial portion of
255 reduction is intracellular (i.e. occurring in periplasmic space)[21]. Therefore, we hypothesize that
256 the site of U(VI) reduction is isolated from the bulk U(VI) solution by a diffusive boundary layer
257 around the cells, impacting the overall "effective" U isotopic fractionation. The generally good
258 reproduction of observed fractionation factors (Fig. 4) as a function of reaction rate by our
259 reactive transport simulations provides support for this hypothesis, as we discuss below.

260 In our models, the concentration difference of U(VI) across the diffusive boundary layer
261 causes U(VI) to diffuse across the barrier. Due to reduction, the U(VI) concentration is lower in
262 the enzyme region and diffusion of U(VI) always occurs from the bulk to the enzyme region.
263 Because the diffusive transport step involves no changes in redox state of U, it does not

264 significantly discriminate between its isotopologues (i.e. ^{238}U(VI) and ^{235}U(VI)) and causes very
265 small isotopic fractionation. It simply controls the availability of the U pool to the reduction step.
266 Therefore, the balance between the kinetics of the diffusion step and the reduction step becomes
267 very important and controls the overall isotopic fractionation. To further discuss this balance, we
268 use two endmember scenarios as examples.
269 First, consider an endmember case of a very rapid enzymatic reduction. Here, diffusion of
270 U(VI) through the boundary layer is the rate-limiting step of all the steps involved in the U(VI)
271 reduction process. The concentrations of both ^{238}U(VI) and ^{235}U(VI) in the remaining U(VI)
272 around the enzyme quickly approach zero. As a consequence, a strong U(VI) concentration
273 gradient develops across the boundary layer and the ratio of the concentration gradients for
274 ^{238}U(VI) and ^{235}U(VI) across the diffusive boundary is close to the ^{238}U(VI)/^{235}U(VI) ratio in the
275 bulk region. Thus, only minor discrimination between ^{238}U and ^{235}U occurs during further
276 diffusive transport. Outside the boundary layer, the ^{238}U(VI)/^{235}U(VI) in the bulk region remains
277 similar to that of the starting U(VI), and only minor effective isotopic fractionation occurs
278 compared to the intrinsic equilibrium ε of ~1‰ caused by the NVE[4,5]. In the second endmember
279 case of extremely slow reduction, diffusion of U(VI) becomes much faster than reduction
280 causing the boundary layer to disappear. As a consequence, the overall isotopic fractionation
281 approaches intrinsic fractionation.
282 In between these endmember cases where diffusion is not fully rate-limiting, slow enzymatic
283 reduction results in accumulation of remaining U(VI) reactant at the inside end of the diffusive
284 boundary layer with an ^{235}U enrichment determined by the intrinsic ε for the reduction. Thus, the
285 overall U(VI) concentration gradient across the boundary layer is less pronounced than in the
286 first endmember case and the ratio of the concentration gradients for ^{238}U(VI) and ^{235}U(VI)

deviates from that in the initial bulk U(VI). This, in turn, causes a relatively enhanced diffusion of ^{238}U(VI) across the boundary layer. In these scenarios, the reduction of U(VI) on the inside end of the diffusive boundary layer will generate an effective isotopic fractionation in the bulk U(VI) that is smaller than the intrinsic equilibrium ε of ~1‰ caused by NVE. Here, the deviation from the intrinsic ε depends on the reduction rate.

Eventually, this coupled kinetic-diffusive effect causes a discrimination of U isotopes during diffusive transport across the boundary layer and hence observable U isotopic fractionation in the bulk region, despite the fact that the diffusivities (i.e. diffusion coefficients) of ^{238}U(VI) and ^{235}U(VI) differ only very slightly. For an additional verification of the consistency of our simulations, the proposed diffusion induced fractionation ($\delta^{238}U_{diff}$) can be quantified as

$$\delta^{238}U_{diff} = \left(\frac{R_{gradient}}{R_{bulk}} - 1 \right) \cdot 1000 \quad ‰ \qquad (1)$$

where $R_{gradient}$ refers to the simulated ^{238}U(VI)/^{235}U(VI) ratio of the net diffusive flux across the diffusive boundary ($R_{gradient}$ = (d^{238}U(VI)/dx)/ (d^{235}U(VI)/dx), with dx = 20 nm, Fig. 1), and R_{bulk} refers to the computed ^{238}U(VI)/^{235}U(VI) concentration ratio in the bulk region. Physically, $\delta^{238}U_{diff}$ corresponds to the theoretical U isotopic ratio of the net U(VI) diffusive flux entering the cell, after having been diffusively transported across the boundary layer and right before the U(VI) reduction step takes place at the enzyme. The computed $\delta^{238}U_{diff}$ values are higher than the simulated δ^{238}U values in the bulk region, and plot on Rayleigh distillation models with effective enrichment factors that are almost identical to the ε derived from the simulated ^{238}U(VI) and ^{235}U(VI) concentrations in the bulk region (shown by the dotted line, Fig. 7). This verifies that the observed and simulated variation in ε (Fig. 2, 7) is mainly due to a preferred diffusion induced fractionation of ^{238}U(VI) across the boundary layer.

309 A similar weakening of isotopic fractionation, sometimes described as reservoir effect, has
310 been reported for reduction Se(VI) in sediments of littoral wetland[10]. This phenomenon arising
311 from diffusive limitations within isolated zones of Se(VI) reduction in sediments lowers the
312 effective ε observed in Se(VI) in overlying water as a function of the distance across which
313 Se(VI) diffuses to the reaction sites. Although the conceptual approach is similar with regards to
314 the isolation of reaction sites in the enzyme region, our data can be explained by a diffusion
315 induced fractionation of U isotopes as described above. Furthermore, in our model we vary the
316 U(VI) reduction rate while keeping the length of the diffusive boundary the same. Note that there
317 is no to back diffusion of ^{235}U enriched U(VI) from the enzyme to the bulk region, which would
318 have to occur against the U concentration gradient. Our results identify U(VI) reaction rate as a
319 crucial factor that controls the effective ε measured in the bulk region.
320 It is possible to invoke the sequestration of U as U(VI) via adsorption on the cells or as U(VI)
321 solid phases inside the cell prior to reduction as an alternative reaction mechanism that may
322 explain our observations of muted isotopic fractionation from *Shewanella* sp. (NR) experiments.
323 U(VI) removal from the solution via adsorption, however, preferentially removes ^{235}U[41,43], which
324 is inconsistent with our data (Fig. 2). Moreover, the adsorption of U(VI) on microbial cells is
325 unlikely to be the major U removal mechanism due to presence of U(VI)-complexing anions (1
326 mM Ca, 10 mM HCO_3^-) and low cell density (~10^7 cells/mL or less) in all of our experiments.
327 Finally, the first order kinetics of U(VI) removal throughout the course of all experiments
328 suggest a single removal mechanism, which is identified as reduction by the XANES data. Even
329 if some of the U(VI) is adsorbed onto the cell at some point in its journey from bulk solution
330 across the boundary layer, any isotopic fractionation in the opposite direction (i.e., ^{238}U
331 enrichment in bulk U(VI)) during this sorption does not affect our interpretation because of the

following reason. Manifestation of U isotopic fractionation in the dissolved U(VI) requires an exchange between U(VI) and U(IV) via reversible weak sorption of U(VI)[24], so eventual desorption reverses any isotopic fractionation caused by sorption of U(VI). Therefore, we conclude that such a sorption effect is likely negligible.

Based on our results, U isotopic fractionation should be influenced by both the rate and the mechanism of U(VI) reduction. Our conceptual model of a diffusive boundary layer around the bacterial cells and simulation results successfully explain how the rate of U(VI) reduction controls U isotopic fractionation during microbial U(VI) reduction. It should be noted that our model does not consider the role of the reduction mechanism in influencing the U isotopic fractionation. The mechanism of U(VI) reduction is likely to vary with reductants with varying electron donating capacity, bonding environment and consequent changes in free energy of the reaction. Previous studies have extended Marcus theory to show that the kinetic isotopic fractionation during redox reactions is related to both reaction kinetics and the vibrational energy differences between reactants and products and thus reaction mechanism and equilibrium fractionation factors[43,44]. According to Marcus theory, the logarithm of the rate constant of redox reactions ($\ln(k)$) varies linearly with the free energy change of the reaction (ΔG_r^0) [43-48]. This means that thermodynamically more favorable reactions at higher $\Delta G_r°$ are faster and have lower activation energy differences between two isotopologues, which should yield smaller fractionation. In future studies, the idea of integrating both the kinetics of electron transfer and equilibrium exchange should be considered to explain overall observed U isotope fractionation[48] in addition to the presence of diffusive boundary layers as we have discussed above. Moreover, it could be assessed whether a coupled kinetic-equilibrium effect as derived from Marcus theory is

354 responsible for observing an equilibrium nuclear volume effect (preference of ^{238}U in U(IV))
355 also in kinetically controlled U(VI) reduction experiments such as in the present study.

356 ***Environmental Implications***

357 Our rate dependent model of microbial U isotope fractionation may be used to interpret
358 environmental U isotope data from a range of settings based on variable abundance of organic
359 matter or electron donors. Our model predicts a small and perhaps variable effective
360 fractionation during active bioremediation experiments where the amended organic carbon
361 enhances the U(VI) reduction rate[9,49]. For instance, this is consistent with a rather low effective ε
362 of 0.46‰ reported for an early stage of the Rifle biostimulation experiment[9]. A recent and more
363 detailed study with a richer dataset at the same site has reported effective ε ranging from 0.65‰
364 to 0.85‰ with changing acetate concentrations (4–15 mM) and hence variable U(VI) reduction
365 rates[25]. Although the correlation between reported ε and U(VI) reduction rate is not perfect
366 because the field experiment is far more complex than a well-mixed batch reactor, this study
367 confirms that U isotopic fractionation does indeed vary at the field-scale when U(VI) reduction
368 rates are changing. In contrast, in natural situations like marine and terrestrial sediments with low
369 organic carbon contents, a slow U(VI) reduction rate should produce a larger fractionation
370 approaching a theoretical NVE value of ~1‰[4,5]. For example, at Smith Ranch-Highlands roll-
371 front deposits, with sub-micromolar dissolved U(VI)[5] and generally low organic C content of the
372 host sediments[50], as well as the lack of a sharp redox gradient evident from a microbial
373 community with diverse and competing metabolism[51], U(VI) reduction is likely slow. This is
374 consistent with a rather high effective ε value of 0.8‰ inferred from variations in the $\delta^{238}U$ of
375 groundwater at the Smith Ranch-Highlands U mine[7] where a significant fraction of the U(VI)
376 reduction is proposed to be microbially mediated[51,52]. The agreement between the fractionation

377 regime suggested by our model at high and low U(VI) reduction rates and the observed ε from
378 the field sites with high and low U(VI) reduction rate demonstrate a systematic relationship
379 between k_{norm} and ε that may be extended to a wider range of natural settings. If either ε or U(VI)
380 reduction rate is directly measured, the systematic relationship may be used to predict the other
381 one. Therefore, direct measurements of U isotope ratios provide a way to quantify U(VI)
382 reduction rate, which is particularly difficult to quantify in modern open systems or in the past
383 environments from the rock record.
384
385 ASSOCIATED CONTENT

386 **Supporting Information**. U(VI) concentration and U isotope results from bacterial incubations,
387 physical and initial chemical parameters for the multi-region model, thermodynamic and kinetic
388 parameters for U(VI) reduction reactions, reaction rate constants to simulate U(VI) reduction,
389 and correlations between normalized U(VI) reduction rate constants and initial U(VI)
390 concentrations are provided in the Supporting Information.

391 AUTHOR INFORMATION

392 **Corresponding Author**

393 * Anirban Basu (Anirban.Basu@rhul.ac.uk), Department of Earth Sciences, 251 Queens
394 Building, Royal Holloway, University of London, Egham, Surrey, UK, TW20 0EX, +44 (0)1784
395 443890; FAX +44 (0) 1784 471 780

396 **Author Contributions**

The manuscript was written through contributions of all authors. All authors have given approval to the final version of the manuscript.

ACKNOWLEDGMENT

This work was supported by the U.S. Department of Energy (USDOE), Office of Science within the Subsurface Biogeochemical Research (SBR) Program under grant DE-SC0001281. We thank the MRCAT/EnviroCAT beamline staff for assistance during XAFS data collection. The XAFS data collection at the Advanced Photon Source and analyses and effort of KMK and MIB were supported by the Argonne Wetlands Hydrobiogeochemistry Scientific Focus Area (SFA) at Argonne National Laboratory funded by the SBR Program, Office of Biological and Environmental Research, Office of Science, USDOE, under contract DE-AC02-06CH11357. MRCAT/EnviroCAT operations are supported by DOE and the MRCAT/EnviroCAT member institutions. We thank the anonymous reviewers for their insightful comments.

REFERENCES

1. Basu, A., Sanford, R. A., Johnson, T. M., Lundstrom, C. C., Löffler, F. E. Uranium isotopic fractionation factors during U(VI) reduction by bacterial isolates. *Geochim. Cosmochim. Acta* **2014,** *136,* 100–113.
2. Stylo, M., Neubert N., Wang, Y., Monga, N., Romaniello, S.J., Weyer, S., Bernier-Latmani, R. Uranium isotopes fingerprint biotic reduction. *Proc. Natl. Acad. Sci. U.S.A.* **2015,** *112*. 5619-5624.
3. Stirling, C. H., Andersen, M. B., Warthmann, R., Halliday, A. N. Isotope fractionation of ^{238}U and ^{235}U during biologically-mediated uranium reduction. *Geochim. Cosmochim. Acta* **2015,** *163*, 200–218.
4. Bigeleisen, J. Nuclear size and shape effects in chemical reactions. Isotope chemistry of the heavy elements. *J. Am. Chem. Soc.* **1996**, *118*, 3676–3680.
5. Fujii, T., Moynier, F., Albarède, F. The nuclear field shift effect in chemical exchange reactions. *Chem. Geol*. **2009,** *267*, 139–156.
6. Basu, A., Brown, S. T., Christensen, J. N., DePaolo, D. J., Reimus, P. W., Heikoop, J.

M., Woldegabriel, G., Simmons, A. M., House, B. M., Hartmann, M., Maher, K. Isotopic and geochemical tracers for U(VI) reduction and U mobility at an in situ recovery U mine. *Environ. Sci. Technol.* **2015**, *49*, 5939–5947.

7. Brown, S. T., Basu, A., Christensen, J. N., Reimus, P. W., Heikoop, J., Simmons, A., Woldegabriel, G., Maher, K., Weaver, K., Clay, J., DePaolo, D. J. Isotopic evidence for reductive immobilization of uranium across a roll-front mineral deposit. *Environ. Sci. Technol.* **2016,** *50*, 6189–6198.
8. Lau, K. V., Maher, K., Altiner, D., Kelley, B. M., Kump, L. R., Lehrmann, D. J., Silva-Tamayo, J. C., Weaver, K. L., Yu, M., Payne, J. L. Marine anoxia and delayed Earth system recovery after the end-Permian extinction. *Proc. Natl. Acad. Sci. U.S.A.* **2016,** *113*, 2360–2365.
9. Bopp, C. J. IV, Lundstrom, C. C., Johnson, T. M., Sanford, R. A., Long, P. E., Williams, K. H. Uranium $^{238}U/^{235}U$ isotope ratios as indicators of reduction: Results from an in situ biostimulation experiment at Rifle, Colorado, U.S.A. *Environ. Sci. Technol.* **2010,** *44*, 5927–5933.
10. Clark, S. K., Johnson, T. M. Effective isotopic fractionation factors for solute removal by reactive sediments: A laboratory microcosm and slurry study. *Environ. Sci. Technol.* **2008,** *42*, 7850–7855.
11. Wiederhold, J. G. Metal stable isotope signatures as tracers in environmental geochemistry. *Environ. Sci. Technol.* **2015**, *49*, 2606–2624.
12. Andersen, M. B., Romaniello, S., Vance, D., Little, S. H., Herdman, R., Lyons, T. W. A modern framework for the interpretation of $^{238}U/^{235}U$ in studies of ancient ocean redox. *Earth Planet. Sci. Lett.* **2014,** *400*, 184–194.
13. Bradley, A. S., Leavitt, W. D., Schmidt, M., Knoll, A. H., Girguis, P. R., Johnston, D. T. Patterns of sulfur isotope fractionation during microbial sulfate reduction. *Geobiology* **2015**, *14*, 91–101.
14. Granger, J., Sigman, D. M., Lehmann, M. F., Tortell, P. D. Nitrogen and oxygen isotope fractionation during dissimilatory nitrate reduction by denitrifying bacteria. *Limnol. Oceanogr.* **2008**, *53*, 2533–2545.
15. Bradley, A. S., Leavitt, W. D., Johnston, D. T. Revisiting the dissimilatory sulfate reduction pathway. *Geobiology* **2011**, 9, 446–457 (2011).
16. Santos, A. A., Venceslau, S. S., Grein, F., Leavitt, W. D., Dahl, C., Johnston, D. T., Pereira, I. A. C. A protein trisulfide couples dissimilatory sulfate reduction to energy conservation. *Science* **2015**, *350*, 1541–1545.
17. Leavitt, W. D., Halevy, I., Bradley, A. S., Johnston, D. T. Influence of sulfate reduction rates on the Phanerozoic sulfur isotope record. *Proc. Natl. Acad. Sci. U.S.A.* **2013,** *110*, 11244–11249.
18. Meyer, T. E., Tsapin, A. I., Vandenberghe, I., Smet, L. D., Frishman, D., Nealson, K. H., Cusanovich, M. A., Van Beeumen, J. J. Identification of 42 possible cytochrome c genes in the *Shewanella oneidensis* genome and characterization of six soluble cytochromes. *OMICS* **2004,** *8*, 57–77.
19. DiChristina, T. J. Enzymology of electron transport: Energy generation with geochemical consequences. *Rev. Mineral. Geochem.* **2005,** *59,* 27–52.
20. DiChristina, T. J., Bates, D. J., Burns, J. L., Dale, J. R., Payne, A. N. *Shewanella*: novel strategies for anaerobic respiration. In *Past and Present Water Column Anoxia;* Neretin, L.N. Ed.; SpringerL: Netherlands, 2006; 443–469.

21. Marshall, M. J., Beliaev, A. S., Dohnalkova, A. C., Kennedy, D. W., Shi, L., Wang, Z., Boyanov, M. I., Lai, B., Kemner, K. M., McLean, J. S., Reed, S. B., Culley, D. E., Bailey, V. L., Simonson, C. J., Saffarini, D. A., Romine, M. F., Zachara, J. M., Fredrickson, J. K. c-type cytochrome-dependent formation of U(IV) nanoparticles by *Shewanella oneidensis*. *Plos Biol.* **2006,** *4*, e268.

22. Wall, J. D., Krumholz, L. R. Uranium reduction. *Annu. Rev. Microbiol*. **2006,** *60,* 149–166.

23. Liu, C., Zachara, J. M., Fredrickson, J. K., Kennedy, D. W., Dohnalkova, A. Modeling the inhibition of the bacterial reduction of U(VI) by β-MnO2(s). *Environ. Sci. Technol.* **2002,** *36*, 1452–1459.

24. Brown, S. T., Basu, A., Ding, X., Christensen, J. N., DePaolo, D. J. Uranium isotope fractionation by abiotic reductive precipitation. *Proc. Natl. Acad. Sci. U.S.A.* **2018,** *115*, 8688–8693.

25. Shiel, A. E., Johnson, T. M., Lundstrom, C. C., Laubach, P. G., Long, P. E., Williams, K. H. Reactive transport of uranium in a groundwater bioreduction study: Insights from high-temporal resolution $^{238}U/^{235}U$ data. *Geochim. Cosmochim. Acta* **2016,** *187*, 218–236.

26. Hyslop, N. P., White, W. H. Estimating precision using duplicate measurements. J. *Air Waste Manag. Assoc.* **2009,** *59,* 1032–1039.

27. Scott, K. M., Lu, X., Cavanaugh, C. M., Liu, J. S. Optimal methods for estimating kinetic isotope effects from different forms of the Rayleigh distillation equation. *Geochim. Cosmochim. Acta* **2004,** *68*, 433–442.

28. Boyanov, M. I., Fletcher, K. E., Kwon, M. J., Rui, X., O'Loughlin, E. J., Löffler, F. E., Kemner, K. M. Solution and microbial controls on the formation of reduced U(IV) species. *Environ. Sci. Technol.* **2011**, *45*, 8336–8344.

29. Xu, T., Sonnenthal, E., Spycher, N. F, Zheng, L. *TOUGHREACT V3.0-OMP Reference manual: a parallel simulation program for non-isothermal multiphase geochemical reactive transport.* Earth Sciences Division, Lawrence Berkeley National Laboratory University of California, Berkeley, CA 94720; http://tough.lbl.gov/assets/docs/TOUGHREACT_V3-OMP_RefManual.pdf.

30. Wolery, T. J. *EQ3/6: software package for geochemical modeling of aqueous systems: package overview and installation guide (version 7.0)*. Lawrence Livermore National Laboratory Report UCRL-MA-110662 PT I. Livermore, California, 1992.

31. Spycher, N. F., Issarangkun, M., Stewart, B. D., Şengör, S. S., Belding, E., Ginn, T. R., Peyton, B. M., Sani, R. K. Biogenic uraninite precipitation and its reoxidation by iron(III) (hydr)oxides: A reaction modeling approach. *Geochim. Cosmochim. Acta* **2011,** *75*, 4426–4440.

32. Wanner, C., Sonnenthal, E. L. Assessing the control on the effective kinetic Cr isotope fractionation factor: A reactive transport modeling approach. *Chem. Geol.* **2013**, *337-338*, 88–98.

33. Singleton, M. J., Sonnenthal, E. L., Conrad, M. E., DePaolo, D. J., Gee, G. W. Multiphase reactive transport modeling of seasonal infiltration events and stable isotope fractionation in unsaturated zone pore water and vapor at the Hanford site. *Vadose Zone J.* **2004,** *3*, 775-785.

34. Wanner, C., Druhan, J. L., Amos, R. T., Alt-Epping, P., Steefel, C. I. Benchmarking the simulation of Cr isotope fractionation. *Comput Geosci* **2014,** *19*, 497–521.

35. Xu, T. Incorporating aqueous reaction kinetics and biodegradation into TOUGHREACT: Applying a multiregion model to hydrobiogeochemical transport of denitrification and sulfate reduction. *Vadose Zone J.* **2008,** 7, 305–315.
36. Abboud, R., Popa, R., Souza-Egipsy, V., Giometti, C. S., Tollaksen, S., Mosher, J. J., Findlay, R. H., Nealson, K. H. Low-temperature growth of *Shewanella oneidensis* MR-1. *Appl. Environ. Microbiol.* **2005,** *7*1, 811–816.
37. Phillips, R. Membranes by the numbers. In *Physics of Biological Membranes; B*assereau, P., Sens, P., Eds.; Springer International Publishing, 2018; pp 73–105.
38. Xiao, Y., Zhang, E., Zhang, J., Dai, Y., Yang, Z., Christensen, H. E. M., Ulstrup, J., Zhao, F. Extracellular polymeric substances are transient media for microbial extracellular electron transfer. *Sci. Adv.* **2017,** *3(7),* e1700623. DOI: 10.1126/sciadv.1700623.
39. Li, S.-W., Sheng, G.-P., Cheng, Y.-Y., Yu, H.-Q. Redox properties of extracellular polymeric substances (EPS) from electroactive bacteria. *Sci. Rep.* **2016,** *6*, 39098. DOI: 10.1038/srep39098.
40. Gao, L., Lu, X., Liu, H., Li, J., Li, W., Song, R., Wang, R., Zhang, D., Zhu, J. Mediation of extracellular polymeric substances in microbial reduction of hematite by *Shewanella Oneidensis* MR-1. *Front. Microbiol.* **2019,** *10*, 575 (2019).
41. Brennecka, G. A., Wasylenki, L. E., Bargar, J. R., Weyer, S., Anbar, A. D. Uranium isotope fractionation during adsorption to Mn-Oxyhydroxides. *Environ. Sci. Technol.* **2011**, *45*, 1370–1375.
42. Jemison, N. E., Johnson, T. M., Shiel, A. E., Lundstrom, C. C. Uranium isotopic fractionation induced by U(VI) adsorption onto common aquifer minerals. *Environ. Sci. Technol.* **2016,** *50*, 12232–12240.
43. Kavner, A., John, S. G., Sass, S., Boyle, E. A. Redox-driven stable isotope fractionation in transition metals: Application to Zn electroplating. *Geochim. Cosmochim. Acta* **2008,** *72*, 1731–1741.
44. Kavner, A., Bonet, F., Shahar, A., Simon, J., Young, E. The isotopic effects of electron transfer: An explanation for Fe isotope fractionation in nature. *Geochim. Cosmochim. Acta* **2005,** *69*, 2971–2979.
45. Marcus, R.A. Chemical and electrochemical electron-transfer theory. *Annu. Rev. Phys. Chem.* **1964,** *15*, 155–196.
46. Marcus, R. A. Electron transfer reactions in chemistry. Theory and experiment. *Rev. Mod. Phys.* **1993,** *65*, 599–610.
47. Marcus, R. A. On the Theory of Electron-Transfer Reactions. VI. Unified Treatment for Homogeneous and Electrode Reactions. *J. Chem. Phys.* **1965,** *43*, 679–701 (1965).
48. Joe-Wong, C., Weaver, K. L., Brown, S. T., Maher, K. Thermodynamic controls on redox-driven kinetic stable isotope fractionation. *Geochem. Persp. Let.* **2019,** *10*, 20–25.
49. Anderson, R. T., Vrionis, H. A., Ortiz-Bernad, I., Resch, C. T., Long, P. E., Dayvault, R., Karp, K., Marutzky, S., Metzler, D. R., Peacock, A., White, D. C., Lowe, M., Lovley, D. R. Stimulating the in situ activity of Geobacter species to remove uranium from the groundwater of a uranium-contaminated aquifer. *Appl. Environ. Microbiol.* **2003,** *69,* 5884–5891.
50. WoldeGabriel, G., Boukhalfa, H., Ware, S. D., Cheshire, M., Reimus, P., Heikoop, J., Conradson, S. D., Batuk, O., Havrilla, G., House, B., Simmons, A., Clay, J., Basu, A., Christensen, J. N., Brown, S. T., DePaolo, D. J. Characterization of cores from an in-situ

recovery mined uranium deposit in Wyoming: Implications for post-mining restoration. *Chem. Geol.* **2013**, *390*, 1–14.

51. Gallegos, T. J., Campbell, K. M., Zielinski, R. A., Reimus, P. W., Clay, J. T., Janot, N., Bargar, J. R., Benzel, W. M. Persistent U(IV) and U(VI) following in-situ recovery (ISR) mining of a sandstone uranium deposit, Wyoming, USA. *Appl. Geochem.* **2015,** *63*, 222–234.

52. Bhattacharyya, A., Campbell, K. M., Kelly, S. D., Roebbert, Y., Weyer, S., Bernier-Latmani, R., Borch, T. Biogenic non-crystalline U(IV) revealed as major component in uranium ore deposits. *Nat. Commun.* **2017**, *8,* 1–8.

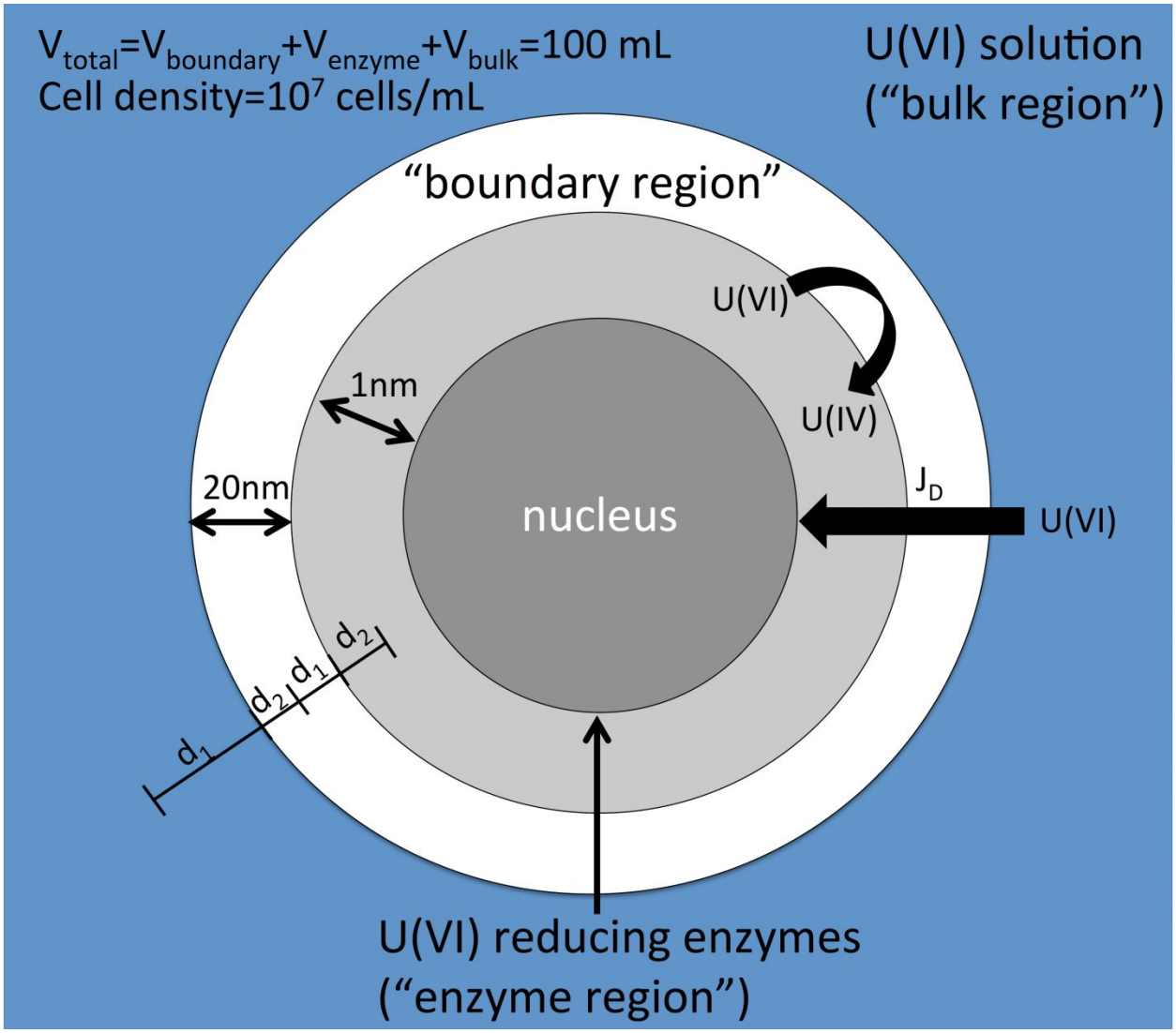

Figure 1. Conceptual model to simulate U(VI) reduction and associated U isotopic fractionation. The model assumes that U(VI) reduction occurs as a two-step process with (i) diffusive U(VI) transport (JD) from the bulk solution (bulk region) to an active site where (ii) enzymatic U(VI) reduction is occurring (enzyme region), which may be at the cell surface or within the periplasmic space. d1 and d2 refer to the distances from the centers of two adjacent regions to their mutual interface (Table S2).

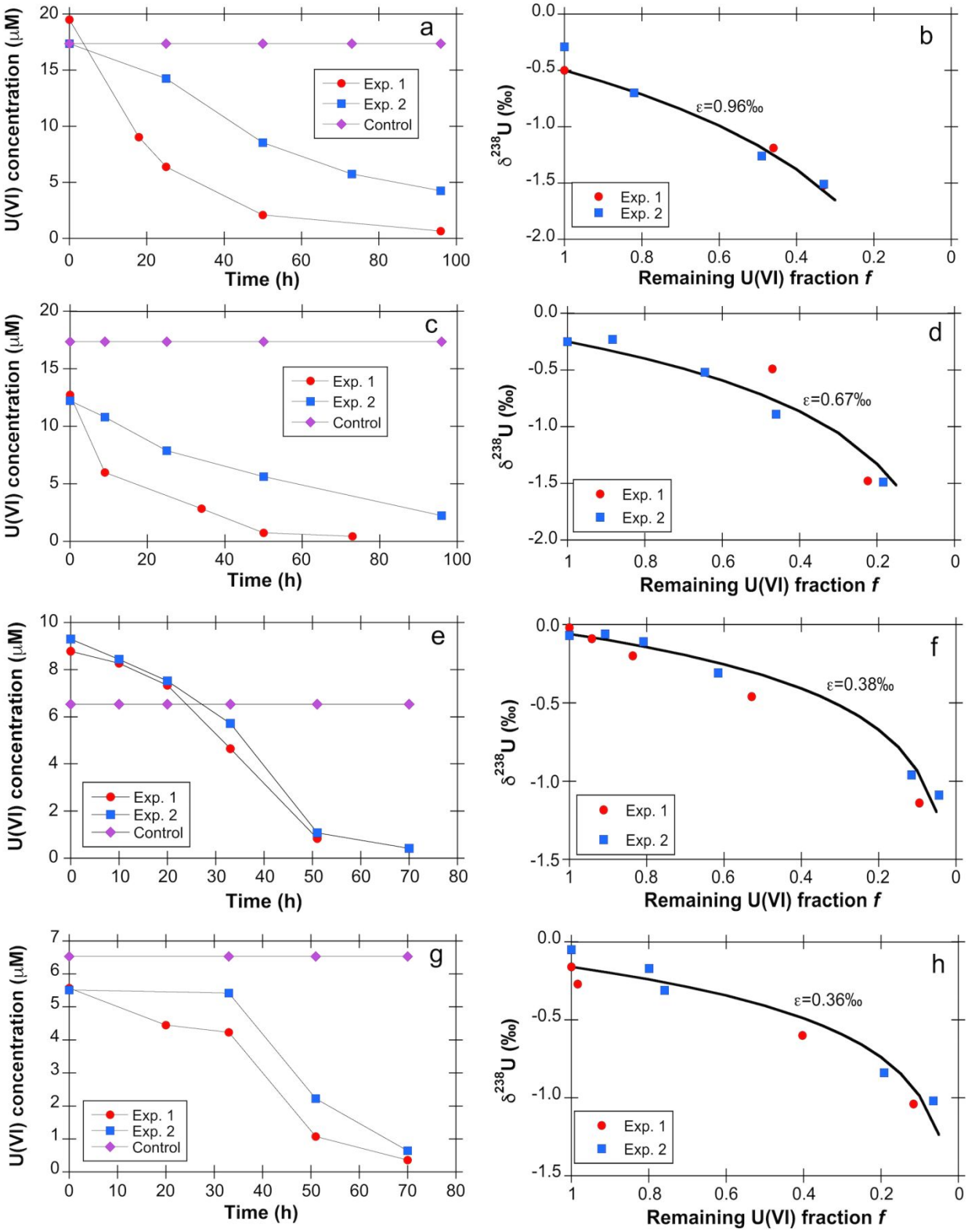
a
U(VI) concentration (μM)
Time (h)
Exp. 1
Exp. 2
Control
b
δ238U (‰)
Remaining U(VI) fraction f
ε=0.96‰
Exp. 1
Exp. 2
c
U(VI) concentration (μM)
Time (h)
Exp. 1
Exp. 2
Control
d
δ238U (‰)
Remaining U(VI) fraction f
ε=0.67‰
Exp. 1
Exp. 2
e
U(VI) concentration (μM)
Time (h)
Exp. 1
Exp. 2
Control
f
δ238U (‰)
Remaining U(VI) fraction f
ε=0.38‰
Exp. 1
Exp. 2
g
U(VI) concentration (μM)
Time (h)
Exp. 1
Exp. 2
Control
h
δ238U (‰)
Remaining U(VI) fraction f
ε=0.36‰
Exp. 1
Exp. 2

584

585

586 **Figure 2.** The left panel shows U(VI) concentration decrease during incubations with
587 *Shewanella* sp. (NR) for U(VI) concentrations a) ~18.2 µM c) ~12.48 µM e) ~9.04 µM g) ~5.54
588 µM. The right panel shows concomitant U isotopic fractionations in b), d), f), h) and j),
589 respectively.
590

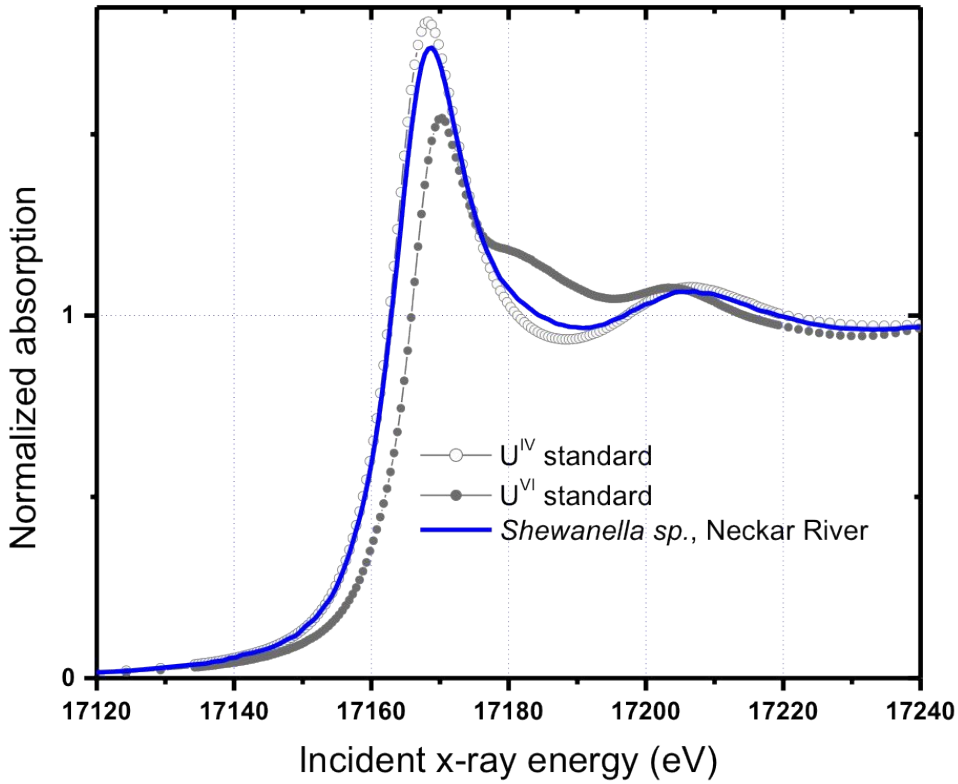

591
592 **Figure 3.** U L_{III}-edge XANES spectrum from the solid phase of incubations with *Shewanella sp.*
593 (NR) (line), compared to U(VI) and U(IV) standards (symbols). The spectrum overlies the U(IV)
594 standard, indicating the predominance of U(IV) species in the sample. The standards are (1)
595 aqueous U(VI)-carbonate species and (2) solid-phase U(IV)-phosphate species produced during
596 U(VI) reduction by *Desulfitobacterium* spp. More information on these standards can be found in
597 ref. [28].

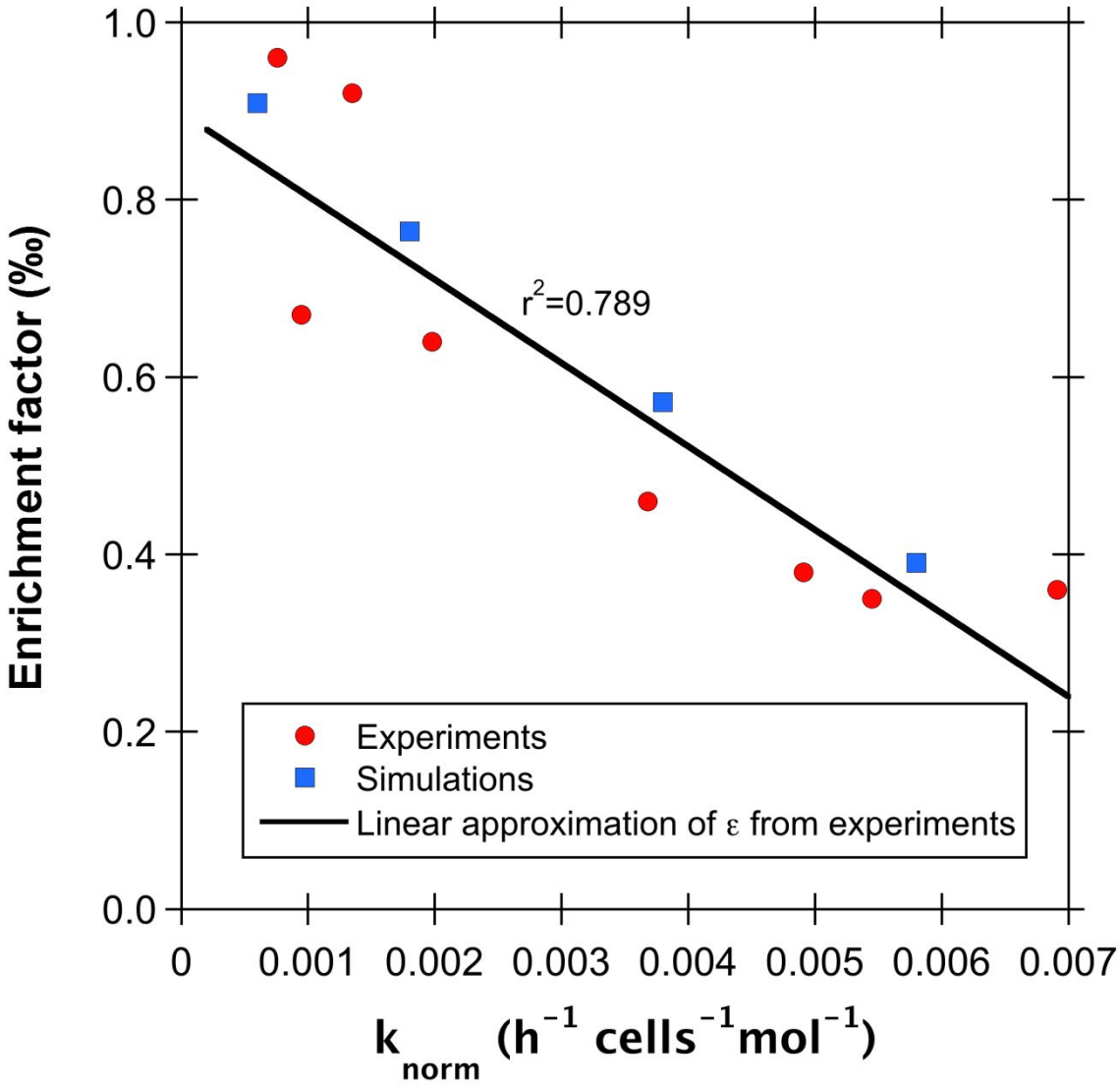

598
599 **Figure 4 .** Correlations in the U(VI) reduction experiments with *Shewanella* sp. (NR): Isotopic
600 fractionation ε vs. normalized rate constant. Also shown are the isotopic fractionation obtained
601 when running the model with different rate constants for different initial U(VI) concentrations
602 and hence variable rate constants.
603

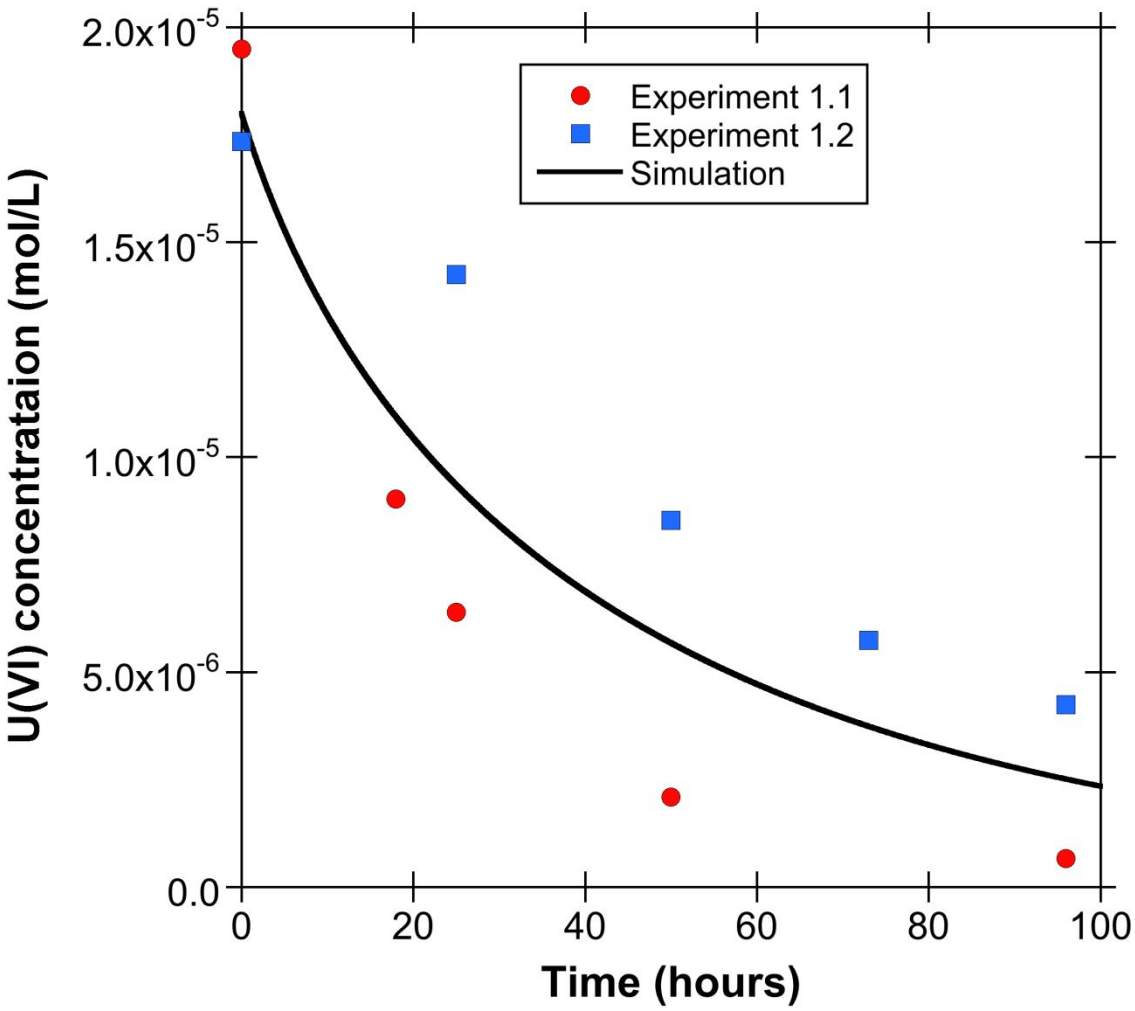

Figure 5. U(VI) concentration as a function of time obtained for an initial U(VI) concentration of ~18 μM and corresponding simulation results (bulk region) illustrating successful calibration of the model.

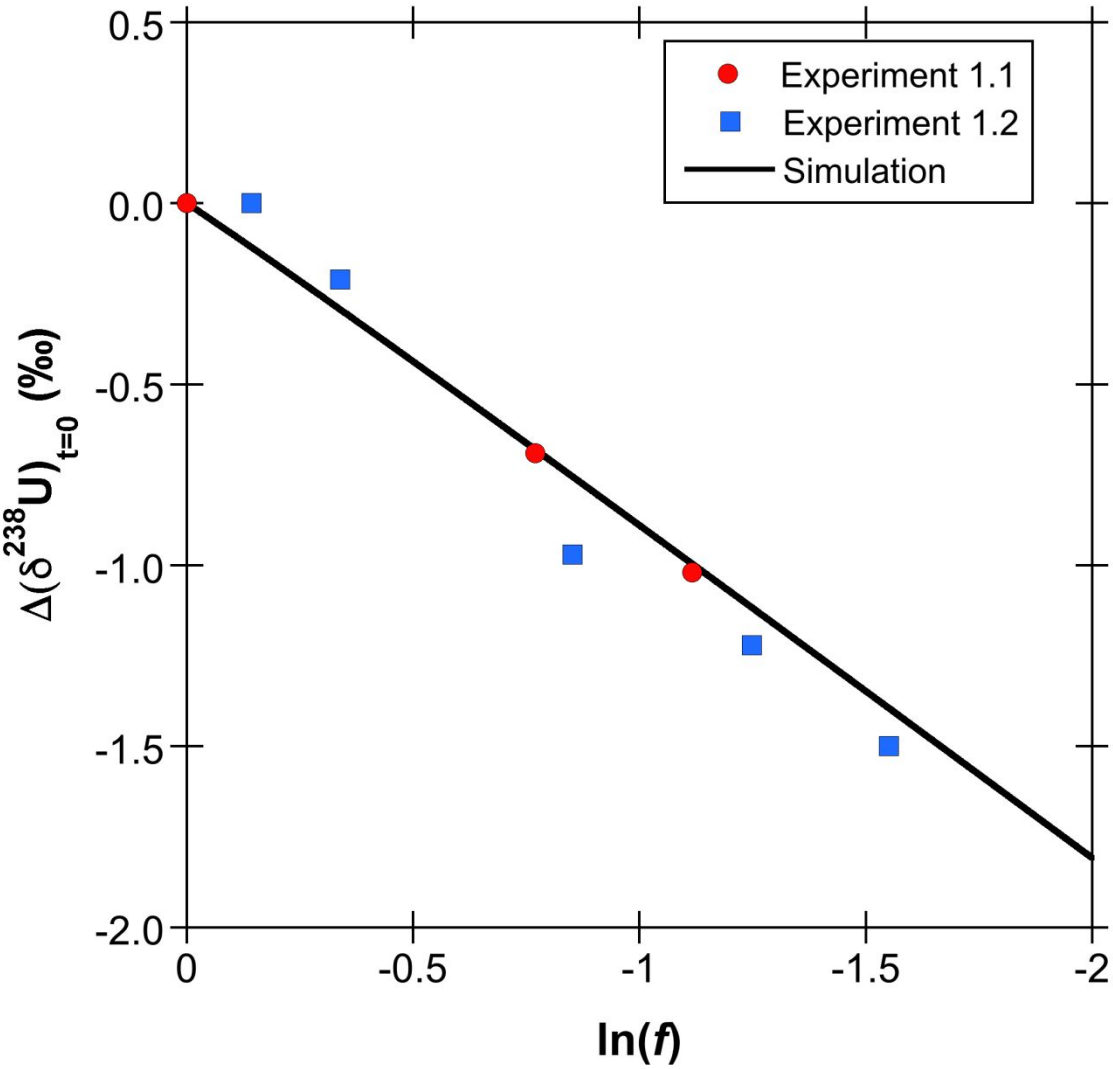

608
609
610 **Figure 6.** Relative $\delta^{238}U$ changes ($\Delta(\delta^{238}U)_{t=0}$) as a function of the natural logarithm of the
611 remaining U(VI) fraction f obtained for an initial U(VI) concentration of ~18 µM and
612 corresponding simulation results (bulk region) illustrating successful model calibration.

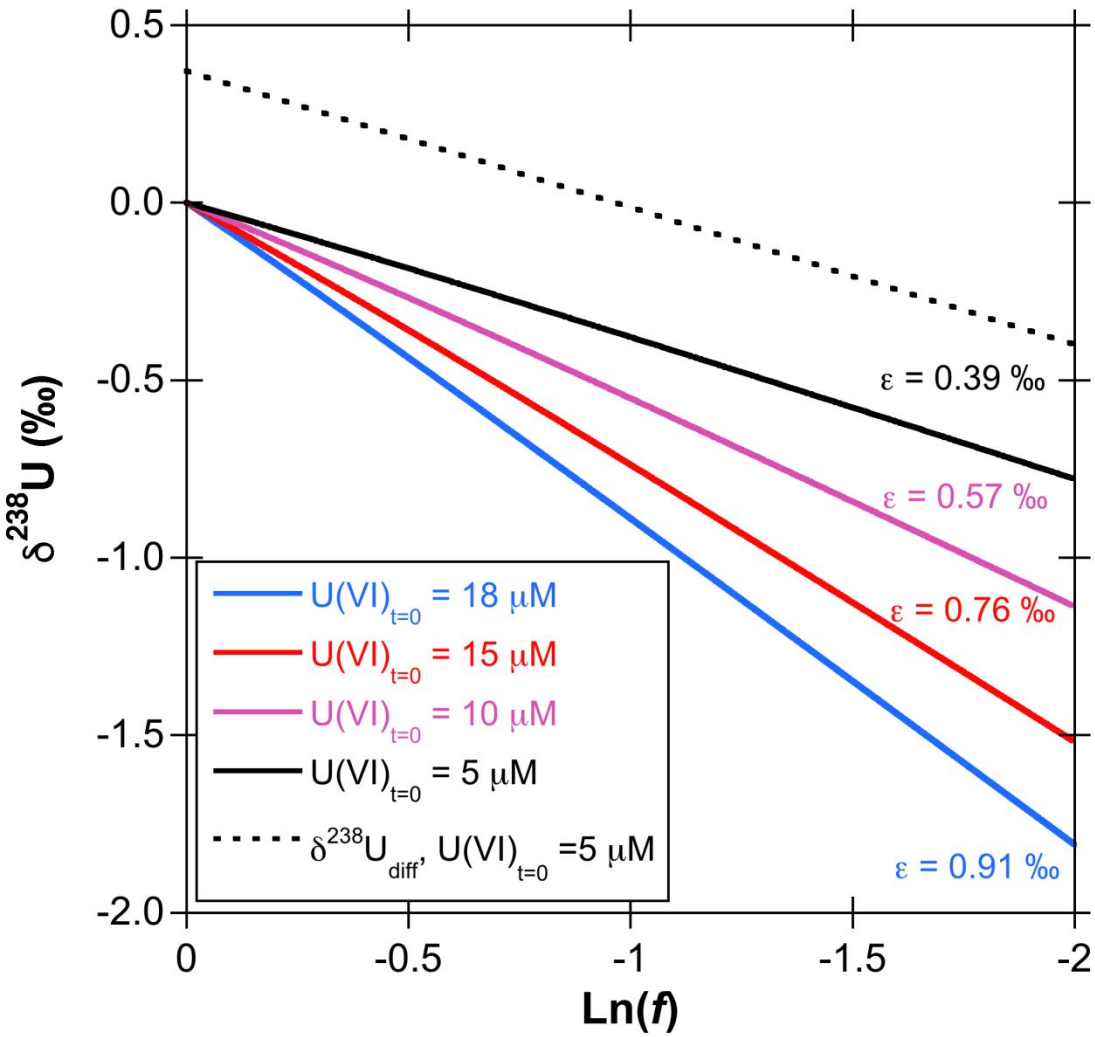

Figure 7. Model results (bulk region) for varying initial U(VI) concentrations. $\delta^{238}U$ values obtained for the bulk region are plotted as a function of the natural logarithm of the remaining U(VI) fraction *f*. All the simulations plot on perfectly straight lines ($r^2=1$), demonstrating that the simulation results follow a Rayleigh type fractionation model with a specific effective epsilon, which is expressed by the corresponding slope. For the simulation with a starting U(VI) concentration of 5 μM, $\delta^{238}U_{diff}$ (eq.(1)) is shown as well to demonstrate that diffusion induced fractionation causes enrichment of $^{238}U(VI)$ across the boundary layer ($\delta^{238}U_{diff} > \delta^{238}U_{bulk}$) and that the corresponding epsilon is equal to the one obtained from the evolution of $\delta^{238}U$ in the bulk solution.